Journal of Vibration Engineering & Technologies (2018) 6:4
https://doi.org/10.1007/s42417-018-0006-7

ORIGINAL PAPER

A State Space Viscoelastic Shaft Finite Element for Stability and Response Analysis of Rotors with Structural and Frequency Dependent Damping

Smitadhi Ganguly[1] · A. Nandi[2] · S. Neogy[2]

Received: 3 October 2015 / Revised: 30 May 2016 / Accepted: 8 June 2016 / Published online: 23 May 2018

Abstract

Objective The present work proposes a new Euler–Bernoulli shaft element for structurally damped and viscoelastic rotors in a spinning frame. The Maxwell–Wiechert linear viscoelastic material model, having one elastic branch and several parallel Maxwell branches, is used. This model introduces additional internal displacement variables between elastic and viscous elements in the Maxwell branches. Here, the stress depends not only on the elastic strain and elastic strain rate but also on additional fictitious strains and their rates.

Methods In the present work, it is assumed that these additional strains can be derived from continuous fictitious displacement variables in the same way as the elastic strains are derived from the actual displacement variables. These continuous fictitious displacements in turn are interpolated from their nodal values using the conventional beam shape functions. Therefore, in addition to the standard degrees of freedom, extra degrees of freedom are defined at the nodes.

Simulation The viscoelastic shaft element is then used in time-domain analysis of rotors with structural damping or frequency-dependent damping. Parameters of the Maxwell–Wiechert model are so selected that they appropriately represent structural damping of a mild steel rotor and frequency-dependent storage modulus and loss coefficient of a typical viscoelastic rotor. Both stability and time response analyses are performed.

Conclusion The results obtained through dynamic analysis of two different rotor models using both structurally damped mild steel and a typical viscoelastic material PPC as shaft material are similar to those available in the literature and justify the methods applied.

Keywords Viscoelastic rotor · Maxwell–Wiechert model · Stability analysis · Time response analysis

Introduction

The elastic moduli of typical viscoelastic materials, namely the storage and loss moduli vary appreciably with frequency. Such materials, therefore, cannot be modeled using the conventional approach used for elastic materials [1–4]. A frequency domain solution may be obtained but the difficulty lies in constructing a time domain formulation. A different approach is needed and a considerable amount of research has already been done in this direction [4–8]. The ATF/ADF model has also been applied in the field of finite element analysis of rotors [9–11]. The GHM method [12] is particularly suitable for using in the domain of finite element analysis. Physically, this method uses additional over-damped oscillators. The inertia, stiffness and damping of the oscillators can be determined from experimental data [13]. More recently, Adhikari [14–19] has studied such energy dissipation in great detail and has coined the term non-viscous damping. Genta and Amati [20] have applied the concept of non-viscous damping to rotating machinery.

The present work proposes a new shaft element derived from the Euler–Bernoulli beam element for viscoelastic rotors in a spinning frame and utilizes it to perform both stability and response analysis of viscoelastic shaft-disc systems. It

✉ Smitadhi Ganguly
smitadhi@hetc.ac.in

A. Nandi
nandi.arghya@gmail.com

S. Neogy
am_sneogy@hotmail.com

[1] Department of Mechanical Engineering, Hooghly Engineering and Technology College, Hooghly, West Bengal 712103, India

[2] Department of Mechanical Engineering, Jadavpur University, Kolkata, West Bengal 700032, India

is well-known that for viscoelastic components subjected to harmonic loading, a frequency-domain analysis is generally attempted. Here one directly uses the frequency-dependent storage modulus and loss coefficient in the material model. However, for other type of loadings, a time dependent viscoelastic material model is essential, particularly in the context of finite element analysis. The Maxwell–Wiechert viscoelastic material model is considered here and a simple technique for incorporating it in a finite element model is presented. This Maxwell–Wiechert finite element model considers additional internal or damping variables between elastic and viscous elements in the Maxwell branches. Here, the stress depends not only on the elastic strain and elastic strain rate but also on additional fictitious strains and their rates. It is considered here that these additional strains can be derived from continuous fictitious displacement variables in the same way as the elastic strains are derived from the actual displacement variables. These continuous fictitious displacements are then interpolated from their nodal values using the conventional beam shape functions. Therefore, in addition to the standard degrees of freedom, extra degrees of freedom are defined at the nodes. If there are m parallel Maxwell branches with m fictitious damping displacements, a single degree of freedom system is converted into a system with $(m+1)$ degrees of freedom. Thus, an originally n degrees of freedom system is converted into a $n(m+1)$ degrees of freedom system. No mass and hence no acceleration is associated with the fictitious displacements. Therefore, when the equations are converted to state space the state variables are only $n(m+2)$. The proposed element can be implemented easily by appropriately appending the usual finite element matrices used for rotor dynamic analysis. Unlike the GHM method, there is no need of elimination of the rigid body modes at the element level.

The present work demands determination of parameters of the Maxwell–Wiechert model for representing the behavior of a viscoelastic material. At the beginning the material model is tested for structural damping, which requires a frequency-independent constant storage modulus and loss coefficient.

Next a conventional viscoelastic material—polypropylene carbonate (PPC) is considered. The parameters of the Maxwell–Wiechert model of PPC are extracted from experimental data. The time domain response analysis is performed using the ODE suite available in MATLAB.

Analysis

A Maxwell–Wiechert model is a standard representation for a viscoelastic material. The Maxwell–Wiechert model has one spring in parallel with a number of parallel Maxwell elements (Fig. 1). A Maxwell element contains a spring and a damper in series. The stress–strain relation for the material can be extracted considering stress as the force and strain as

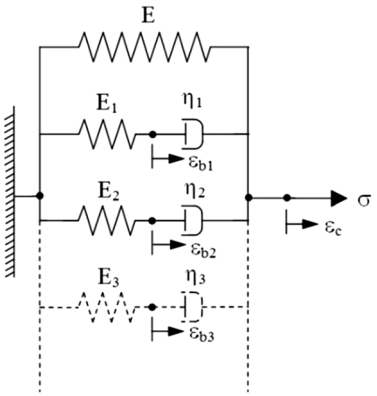

Fig. 1 The Maxwell–Wiechert model with three Maxwell branches

displacement in this spring-damper combination. In each Maxwell branch, an additional fictitious damping degree of freedom is considered between the spring and the damper.

The stress–strain relation for the viscoelastic material is expressed as follows:

$$\sigma = E\varepsilon_c + \eta_1\left(\dot{\varepsilon}_c - \dot{\varepsilon}_{b1}\right) + \eta_2\left(\dot{\varepsilon}_c - \dot{\varepsilon}_{b2}\right), \tag{1}$$

$$\eta_1\left(\dot{\varepsilon}_c - \dot{\varepsilon}_{b1}\right) = E_1\varepsilon_{b1}, \tag{2}$$

$$\eta_2\left(\dot{\varepsilon}_c - \dot{\varepsilon}_{b2}\right) = E_2\varepsilon_{b2}. \tag{3}$$

It is assumed that like the actual strain ε_c, the additional variables ε_{bi} as shown in Fig. 1, can be obtained from additional displacement-like variables w_{by} and w_{bz}.

$$\varepsilon_c = -\left(y\frac{\partial^2 w_{cy}}{\partial x^2} + z\frac{\partial^2 w_{cz}}{\partial x^2}\right), \tag{4a}$$

$$\varepsilon_b = -\left(y\frac{\partial^2 w_{by}}{\partial x^2} + z\frac{\partial^2 w_{bz}}{\partial x^2}\right). \tag{4b}$$

For an Euler–Bernoulli beam, while the actual strain is determined from the relation (4a), the additional strain can be determined from additional continuous displacement variables w_{by} and w_{bz} (Eq. 4b).

For finite element formulation the virtual work principle is adopted. The virtual strain energy is equal to the virtual work done by the inertia force, gyroscopic force and external force. The formulation is attempted in the spinning frame. Therefore, the expressions for inertia and gyroscopic forces in spinning frame are considered. The stress, strain and external forces are all considered with respect to the spinning frame.

The virtual strain energy per unit volume

$$= \delta\varepsilon_c\sigma = \delta\varepsilon_c\left\{E\varepsilon_c + \eta_1\left(\dot{\varepsilon}_c - \dot{\varepsilon}_{b1}\right) + \eta_2\left(\dot{\varepsilon}_c - \dot{\varepsilon}_{b2}\right)\right\}. \tag{5}$$

It is assumed that just like the actual displacements w_{cy} and w_{cz} are interpolated from the eight nodal variables $\{U_c\}$

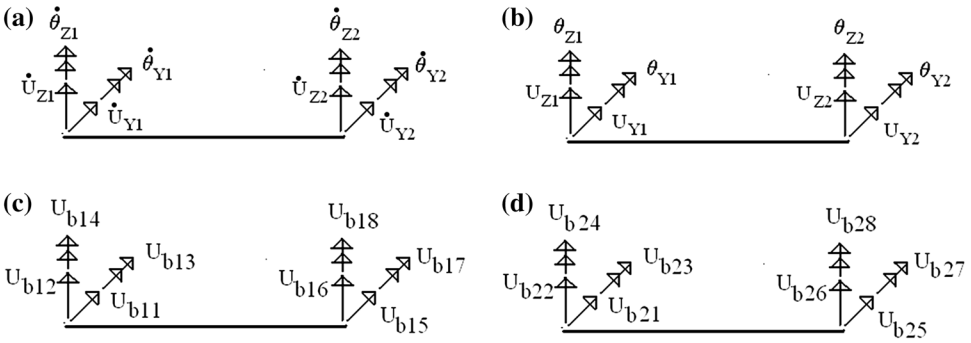

Fig. 2 Degrees of freedom of the proposed element with two Maxwell branches are composed of **a** velocity degrees of freedom, **b** usual degrees of freedom, **c** damping degrees of freedom for the first Maxwell branch, **d** damping degrees of freedom for the second Maxwell branch

(2 displacements and 2 rotations at each node), the additional displacement-like variables w_{by} and w_{bz} are also interpolated from another eight additional nodal variables $\{U_b\}$ (Fig. 2).

$$\varepsilon_c = [B]\{U_c\}; \quad \varepsilon_b = [B]\{U_b\}. \tag{6}$$

The matrix $[B]$ is the standard strain–displacement matrix for three-dimensional Euler–Bernoulli beam element.

Now, the virtual strain energy per unit volume

$$\begin{aligned}\delta\varepsilon_c\sigma &= \{\delta U_c\}^T[B]^T\{E[B]\{U_c\} + \eta_1[B](\{\dot{U}_c\} \\ &\quad -\{\dot{U}_{b1}\}) + \eta_2[B](\{\dot{U}_c\} - \{\dot{U}_{b2}\})\} \\ &= \{\delta U_c\}^T[B]^T E[B]\{U_c\} \\ &\quad + \{\delta U_c\}^T[B]^T(\eta_1+\eta_2)[B]\{\dot{U}_c\} \\ &\quad - \{\delta U_c\}^T[B]^T\{\eta_1\{\dot{U}_{b1}\} + \eta_2\{\dot{U}_{b1}\}\}.\end{aligned} \tag{7}$$

The virtual work done by the inertia force and gyroscopic moment in the spinning frame can be written as

$$\begin{aligned}&-\{\delta U_c\}^T(([M_T^e] + [M_R^e])\{\ddot{U}_c\} \\ &+2\omega[\hat{M}_T^e]\{\dot{U}_c\} \\ &-\omega^2([M_T^e] - [M_R^e])\{U_c\}).\end{aligned} \tag{8}$$

The inertia force and gyroscopic moment can be first derived in the inertial frame and then transformed to spinning frame. Alternatively one can obtain the velocity and kinetic energy expressions in spinning frame [21]. The inertia and gyroscopic terms can be obtained by taking the first variation of the kinetic energy.

The work done by the external forces is

$$\{\delta U_c\}^T\{f^e\}. \tag{9}$$

Now, the following notations can be used:

$$[M^e] = [M_T^e] + [M_R^e], \tag{10a}$$

$$[G^e] = 2\omega[\hat{M}_T^e], \tag{10b}$$

$$[K_1^e] = -\omega^2([M_T^e] - [M_R^e]). \tag{10c}$$

Using the virtual work principle one obtains

$$\begin{aligned}&\{\delta U_c\}^T\Bigg\{[M^e]\{\ddot{U}_c\} + [G^e]\{\dot{U}_c\} + [K_1^e]\{U_c\} \\ &+\int_V [B]^T E[B]dV\{U_c\} + \int_V [B]^T(\eta_1+\eta_2)[B]dV\{\dot{U}_c\} \\ &-\left\{\int_V [B]^T\eta_1[B]dV\{\dot{U}_{b1}\} + \int_V [B]^T\eta_2[B]dV\{\dot{U}_{b2}\}\right\}\Bigg\} \\ &= \{\delta U_c\}^T\{f^e\}.\end{aligned} \tag{11}$$

Considering

$$[\bar{K}^e] = \int_V [B]^T[B]\mathrm{d}V, \tag{12}$$

$$\begin{aligned}&[M^e]\{\ddot{U}_c\} + [G^e]\{\dot{U}_c\} + (\eta_1+\eta_2)[\bar{K}^e]\{\dot{U}_c\} \\ &\quad -\{\eta_1[\bar{K}^e]\{\dot{U}_{b1}\} + \eta_2[\bar{K}^e]\{\dot{U}_{b2}\}\} \\ &\quad + E[\bar{K}^e]\{U_c\} + [K_1^e]\{U_c\} = \{f^e\}.\end{aligned} \tag{13}$$

For each Maxwell branch the stress in the elastic part is same as the stress in the damping part. Therefore, after pre-multiplying by $\delta\varepsilon_c = [B]\{\delta U_c\}$, the following relation holds for the first Maxwell branch.

$$\begin{aligned}&\{\delta U_c\}^T\int_V -[B]^T\eta_1[B]dV\{\dot{U}_c\} + \{\delta U_c\}^T\int_V [B]^T\eta_1[B]dV\{\dot{U}_{b1}\} \\ &\quad + \{\delta U_c\}^T\int_V [B]^T E_1[B]dV\{U_{b1}\} = \{0\}.\end{aligned} \tag{14}$$

Or, using relation (12) the constraint equations for two Maxwell branches are as follows:

$$-\eta_1\left[\bar{K}^e\right]\left\{\dot{U}_c\right\}+\eta_1\left[\bar{K}^e\right]\left\{\dot{U}_{b1}\right\}+E_1\left[\bar{K}^e\right]\left\{U_{b1}\right\}=\{0\},\quad(15a)$$

$$-\eta_2\left[\bar{K}^e\right]\left\{\dot{U}_c\right\}+\eta_2\left[\bar{K}^e\right]\left\{\dot{U}_{b2}\right\}+E_2\left[\bar{K}^e\right]\left\{U_{b2}\right\}=\{0\}.\quad(15b)$$

Combining the above equations one obtains

$$\begin{bmatrix}[M^e] & [0] & -\eta_1[\bar{K}^e] & -\eta_2[\bar{K}^e]\\ [0] & [I] & [0] & [0]\\ [0] & [0] & \eta_1[\bar{K}^e] & [0]\\ [0] & [0] & [0] & \eta_2[\bar{K}^e]\end{bmatrix}\begin{Bmatrix}\{\ddot{U}_c\}\\ \{\dot{U}_c\}\\ \{\dot{U}_{b1}\}\\ \{\dot{U}_{b2}\}\end{Bmatrix}$$
$$+\begin{bmatrix}(\eta_1+\eta_2)\left[\bar{K}^e\right]+[G^e] & E[\bar{K}^e]+\left[K_1^e\right] & [0] & [0]\\ -[I] & [0] & [0] & [0]\\ -\eta_1[\bar{K}^e] & [0] & E_1[\bar{K}^e] & [0]\\ -\eta_2[\bar{K}^e] & [0] & [0] & E_2[\bar{K}^e]\end{bmatrix}\begin{Bmatrix}\{\dot{U}_c\}\\ \{U_c\}\\ \{U_{b1}\}\\ \{U_{b2}\}\end{Bmatrix}=\begin{Bmatrix}\{f^e\}\\ \{0\}\\ \{0\}\\ \{0\}\end{Bmatrix}.\quad(16a)$$

If there are three Maxwell branches the state space equations are as follows:

$$\begin{bmatrix}[M^e] & [0] & -\eta_1[\bar{K}^e] & -\eta_2[\bar{K}^e] & -\eta_3[\bar{K}^e]\\ [0] & [I] & [0] & [0] & [0]\\ [0] & [0] & \eta_1[\bar{K}^e] & [0] & [0]\\ [0] & [0] & [0] & \eta_2[\bar{K}^e] & [0]\\ [0] & [0] & [0] & [0] & \eta_3[\bar{K}^e]\end{bmatrix}\begin{Bmatrix}\{\ddot{U}_c\}\\ \{\dot{U}_c\}\\ \{\dot{U}_{b1}\}\\ \{\dot{U}_{b2}\}\\ \{\dot{U}_{b3}\}\end{Bmatrix}$$
$$+\begin{bmatrix}(\eta_1+\eta_2+\eta_3)\left[\bar{K}^e\right]+[G^e] & E[\bar{K}^e]+\left[K_1^e\right] & [0] & [0] & [0]\\ -[I] & [0] & [0] & [0] & [0]\\ -\eta_1[\bar{K}^e] & [0] & E_1[\bar{K}^e] & [0] & [0]\\ -\eta_2[\bar{K}^e] & [0] & [0] & E_2[\bar{K}^e] & [0]\\ -\eta_3[\bar{K}^e] & [0] & [0] & [0] & E_3[\bar{K}^e]\end{bmatrix}\begin{Bmatrix}\{\dot{U}_c\}\\ \{U_c\}\\ \{U_{b1}\}\\ \{U_{b2}\}\\ \{U_{b3}\}\end{Bmatrix}$$
$$=\begin{Bmatrix}\{f^e\}\\ \{0\}\\ \{0\}\\ \{0\}\\ \{0\}\end{Bmatrix}.\quad(16b)$$

Determination of the Parameters of the Parallel Maxwell Elements

The real and imaginary parts of the material modulus can be computed using the following relations derived from the Maxwell–Wiechert model with three parallel branches:

$$E_s=E+\frac{E_1\omega^2\tau_1^2}{1+\omega^2\tau_1^2}+\frac{E_2\omega^2\tau_2^2}{1+\omega^2\tau_2^2}+\frac{E_3\omega^2\tau_3^2}{1+\omega^2\tau_3^2},\quad(17a)$$

$$E_I=\frac{E_1\omega\tau_1}{1+\omega^2\tau_1^2}+\frac{E_2\omega\tau_2}{1+\omega^2\tau_2^2}+\frac{E_3\omega\tau_3}{1+\omega^2\tau_3^2},\quad(17b)$$

where

$$\tau_i=\frac{\eta_i}{E_i}\quad i=1,2,3,\quad(17c)$$

the E_i's and η_i's being stiffness and damping parameters of the three parallel Maxwell branches and their ratio τ_i's are the relaxation parameters.

The loss coefficient is given by

$$\eta=\frac{E_I}{E_s}.\quad(17d)$$

The stiffness and damping parameters of the parallel Maxwell branches can be determined by curve-fitting Eq. 17a and 17b to available complex modulus data of particular materials. The Maxwell–Wiechert model can not only be used to approximate the complex modulus of the viscoelastic materials but also the structural damping phenomenon found in most metals. Here an effort has been made to fit the parallel Maxwell branch parameters to model the viscoelastic materials as well as structural damping.

The characteristic of structural damping [22] is that both the storage modulus and loss coefficient remains constant with change in frequency. It has been observed that the contribution of each parallel branch to the imaginary part of the material modulus peaks at a frequency equal to $\frac{1}{\tau_i}$. If we assume that the real part E_S is essentially the elasticity modulus E and the imaginary part E_I is a constant ηE then, depending upon the range of frequency that is of interest, three different frequencies ω_i can be picked ($\omega_i=1/\tau_i$) at each of which one of the three branches works at its peak damping condition. If the sum of all the terms in 22b is made equal to ηE at those three chosen frequencies (ω_i) then the necessary condition for structural damping is achieved. To simplify the calculations it is generally assumed that the ω_i's are in geometric progression with a common ratio r. Therefore, for a chosen ω_2

$$\omega_1=\frac{\omega_2}{r},\omega_3=\omega_2 r.\quad(17e)$$

Further it can be assumed that

$$E_i=\alpha_i E\quad i=1,2,3.\quad(17f)$$

So, three linear equations in unknown α_i's containing three predetermined ω_i's ($\omega_i=1/\tau_i$) are obtained as follows:

$$\left.\begin{aligned}\frac{\alpha_1\omega_1^2}{\omega_1^2+\omega_1^2}+\frac{\alpha_2\omega_1\omega_2}{\omega_2^2+\omega_1^2}+\frac{\alpha_3\omega_1\omega_3}{\omega_3^2+\omega_1^2}&=\eta\\ \frac{\alpha_1\omega_1\omega_2}{\omega_1^2+\omega_2^2}+\frac{\alpha_2\omega_2^2}{\omega_2^2+\omega_2^2}+\frac{\alpha_3\omega_2\omega_3}{\omega_3^2+\omega_2^2}&=\eta\\ \frac{\alpha_1\omega_1\omega_3}{\omega_1^2+\omega_3^2}+\frac{\alpha_2\omega_2\omega_3}{\omega_2^2+\omega_3^2}+\frac{\alpha_3\omega_3^2}{\omega_3^2+\omega_3^2}&=\eta\end{aligned}\right\}.\quad(17g)$$

Assuming a value of $r=10$ and $\eta=0.01$ for mild steel with $E=2\times10^{11}$ Pa the stiffness and damping parameters of the three parallel Maxwell elements have been calculated in the reference range of (30–3000) rad/s and are listed in Table 1. The same procedure has been repeated for one/two parallel Maxwell branches and the parameters obtained are listed in Tables 2 and 3. Using the parameters for three parallel Maxwell branches the storage modulus and loss coefficients are plotted against non-dimensional frequency in log scale showing the contribution of each of the three branches as well as against frequency in linear scale in Fig. 3.

For typical viscoelastic materials like polymers both the storage modulus and loss coefficient vary appreciably with frequency. There is no direct algebraic solution for extraction of the branch parameters. A relevant frequency range can be taken. An initial guess of the unknowns may be assumed from which a set of parameters giving fair approximation of the actual data may be obtained through optimization. Here a common viscoelastic material PPC is used. The elastic modulus data for this viscoelastic material are obtained through specimen testing in the laboratory. The parameters of the Maxwell–Wiechert model with three parallel branches are then extracted by curve-fitting the test data and are listed in Table 4.

Validation

Though the objective of the present work is time-domain analysis, a harmonic analysis can be attempted just for the sake of validation of the state-space equations.

There are now two alternative ways for computing the frequency response. The usual way is to start with the governing equations without any additional damping degrees of freedom. The element equations are assembled to obtain the following equations for the system.

$$[M]\{\ddot{U}\}+[G]\{\dot{U}\}++E[\bar{K}]\{\dot{U}\}+[K_1]\{U\}=\{F\}. \quad (18)$$

Assuming harmonic excitation in the form $\{F\}=\{F_0\}e^{j\omega t}$, the displacement and material modulus are written as follows:

$$\{U\}=\{U_0\}e^{j\omega t}, \quad (19)$$

$$E=E_s(\omega)(1+j\eta(\omega)), \quad (20a)$$

$$E=E_S(\omega)+jE_I(\omega), \quad (20b)$$

where

$$E_I(\omega)=E_s(\omega)\eta(\omega). \quad (20c)$$

Table 2 Values of parameters in a two-parallel element Maxwell–Wiechert model for structural damping of MS with $\eta=0.01$

Material	E (N/m^2)	E_1 (N/m^2)	E_2 (N/m^2)	η_1 (Ns/m^2)	η_2 (Ns/m^2)
Mild steel	2.0×10^{11}	3.339×10^9	3.339×10^9	3.339×10^7	3.339×10^6

Table 3 Values of parameters in a one-parallel element Maxwell–Wiechert model for structural damping of MS with $\eta=0.01$

Material	E (N/m^2)	E_1 (N/m^2)	η_1 (Ns/m^2)
Mild steel	2.0×10^{11}	4.0×10^9	1.333×10^7

The material modulus is expressed as a frequency-dependent complex number in terms of storage modulus and loss coefficient. The displacement $\{U_0\}$ is a complex number and can be determined from the following equation:

$$\{U_0\}=\{E_s(\omega)(1+j\eta(\omega))[\bar{K}]-\omega^2[M]+j\omega[G]\}^{-1}\{F_0\}. \quad (21)$$

The alternative starts with the state space form with additional damping degrees of freedom. The element equations are shown in Eq. (16). Equation (16a) or (16b) can be assembled and written as follows:

$$[A]\{\dot{Z}\}+[B]\{Z\}=\{R\}. \quad (22)$$

Considering $\{R\}=\{R_0\}e^{j\omega t}$ and $\{Z\}=\{Z_0\}e^{j\omega t}$, one obtains

$$\{Z_0\}=(j\omega[A]+[B])^{-1}\{R_0\}. \quad (23)$$

Results computed from Eqs. (21) and (23) are compared for the purpose of validation. A close match ascertains the correctness of the state space matrices $[A]$ and $[B]$.

Two different simply supported rotor-disc systems are used in the numerical study to model both structural damping and frequency dependent viscoelastic behaviour. The first system has a single rigid disc while the second system used two rigid discs on a simply supported shaft. Mild steel is used as rotor material in case of structural damping with a loss coefficient of 0.01. The case of mild steel is only considered to test the applicability of the Maxwell–Wiechert model for structural damping. A commonly used viscoelastic material PPC is used for the other one.

Table 1 Values of parameters in a three-parallel element Maxwell–Wiechert model for structural damping of MS with $\eta=0.01$

Material	E (N/m^2)	E_1 (N/m^2)	E_2 (N/m^2)	E_3 (N/m^2)	η_1 (Ns/m^2)	η_2 (Ns/m^2)	η_3 (Ns/m^2)
Mild steel	2.0×10^{11}	3.407×10^9	2.651×10^9	3.407×10^9	1.136×10^8	8.836×10^6	1.136×10^6

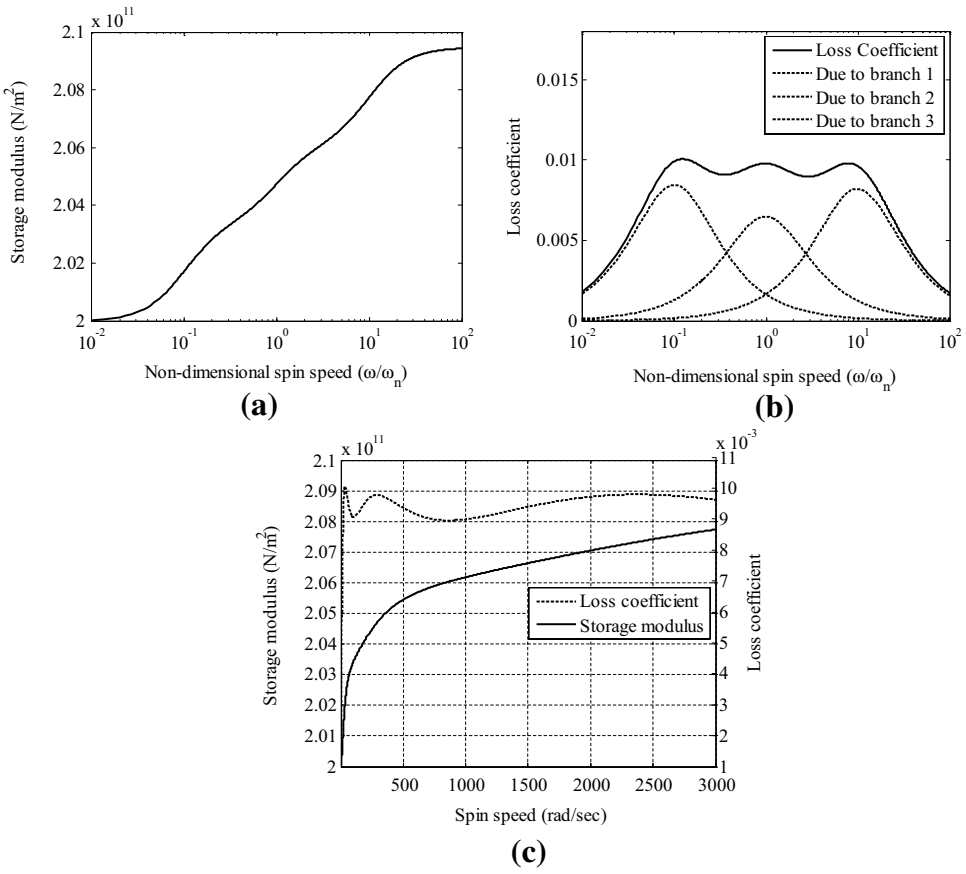

Fig. 3 Plots of **a** storage modulus, **b** loss coefficient (showing the contribution of each branch) obtained using three parallel branches against non-dimensional spin speed in log scale **c** storage modulus and loss coefficient against spin speed in the reference range

Table 4 Values of the extracted parameters in a three-parallel element Maxwell–Wiechert model for PPC

Material	E (N/m^2)	E_1 (N/m^2)	E_2 (N/m^2)	E_3 (N/m^2)	η_1 (Ns/m^2)	η_2 (Ns/m^2)	η_3 (Ns/m^2)
PPC	1.28×10^9	1.104×10^8	5.469×10^7	1.986×10^8	1.087×10^7	3.879×10^5	1.205×10^5

Rotor-Disc System 1 A rotor of 600 mm length and 15 mm diameter is considered (Fig. 4). The disc has 1 kg mass and 100 mm radius of gyration corresponding to polar moment of inertia. The rotor shaft is simply supported with the disc located at a distance of 400 mm from the left end support.

Rotor-Disc System 2 A rotor of 600 mm length and 20 mm diameter and fitted with two discs is considered (Fig. 5). Both discs have a mass of 1 kg and 100 mm radius of gyration corresponding to polar moment of inertia. The rotor shaft is simply supported with the two discs located at distances of 200 and 400 mm from the left end support respectively.

For the validation examples, the spin speed is kept zero. A harmonic force of amplitude 1 N and varying frequency is applied at the location of the single disc in the first model and the left disc in the second model. A Maxwell–Wiechert model with three Maxwell branches has been used.

Here both systems use mild steel as the shaft material to model structural damping. The frequency response plots computed using Eqs. (21) and (23) are compared in Fig. 6. They are found to be identical with exactly same location and amplitude of the peaks.

The viscoelastic material data of PPC are used to obtain the frequency response plots of the two systems. The plots (Fig. 7) show that the two approaches elicit identical response as in the previous case.

Numerical Study in Time Domain

The state space model developed here can be used for stability analysis. For stability analysis, the eigenvalues of the homogeneous part of Eq. (22) are computed over a

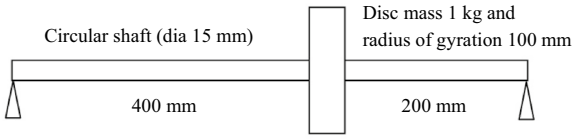

Fig. 4 Rotor-disc system 1

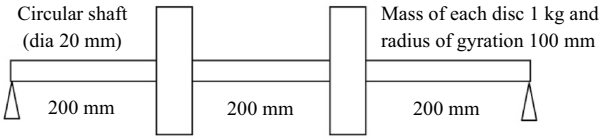

Fig. 5 Rotor-disc system 2

frequency range. The largest real part of the eigenvalues and the Campbell Diagram for the first mode is plotted for both rotor-disc systems considering a structurally damped mild steel rotor as well as a viscoelastic rotor. In the presence of rotating non-viscous damping the largest real part becomes positive beyond a certain spin speed equal to the forward synchronous whirl frequency and renders the rotor-disc system unstable. The same rotors as those shown in Figs. 4 and 5 are considered for analysis.

The stability plots of mild steel rotor are computed using one, two and three parallel Maxwell branches and the results are compared. It is observed that the model with three parallel branches gives the most satisfactory representation of structural damping for both systems (Figs. 8, 9).

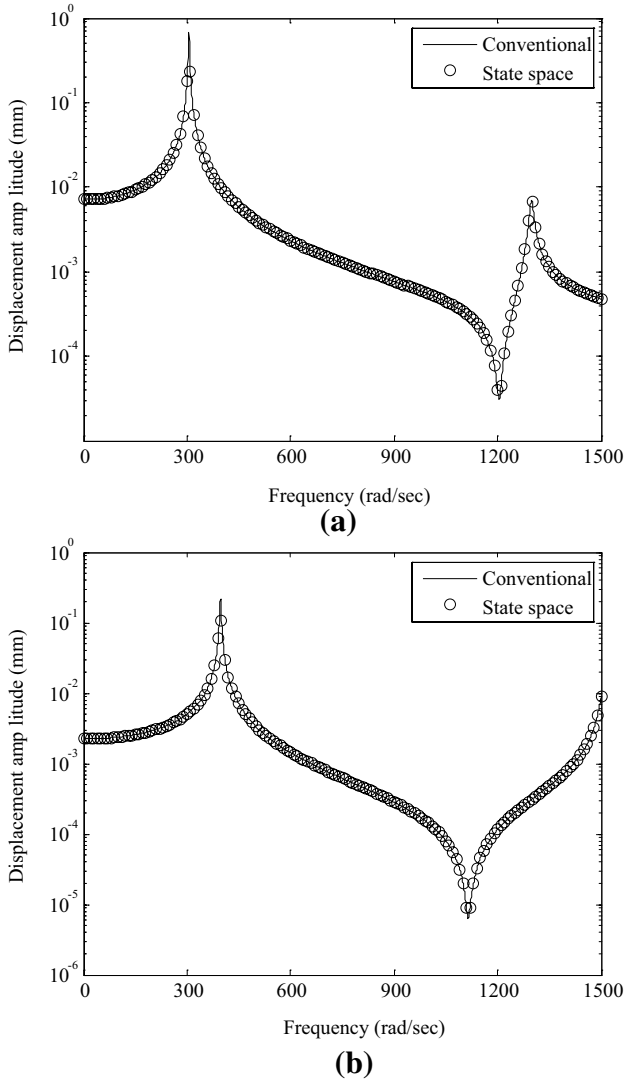

Fig. 6 Frequency response computed using conventional frequency-dependent storage modulus and loss coefficient and state space viscoelastic model with additional degrees of freedom for **a** rotor-disc system 1, **b** rotor-disc system 2 using mild steel as shaft material

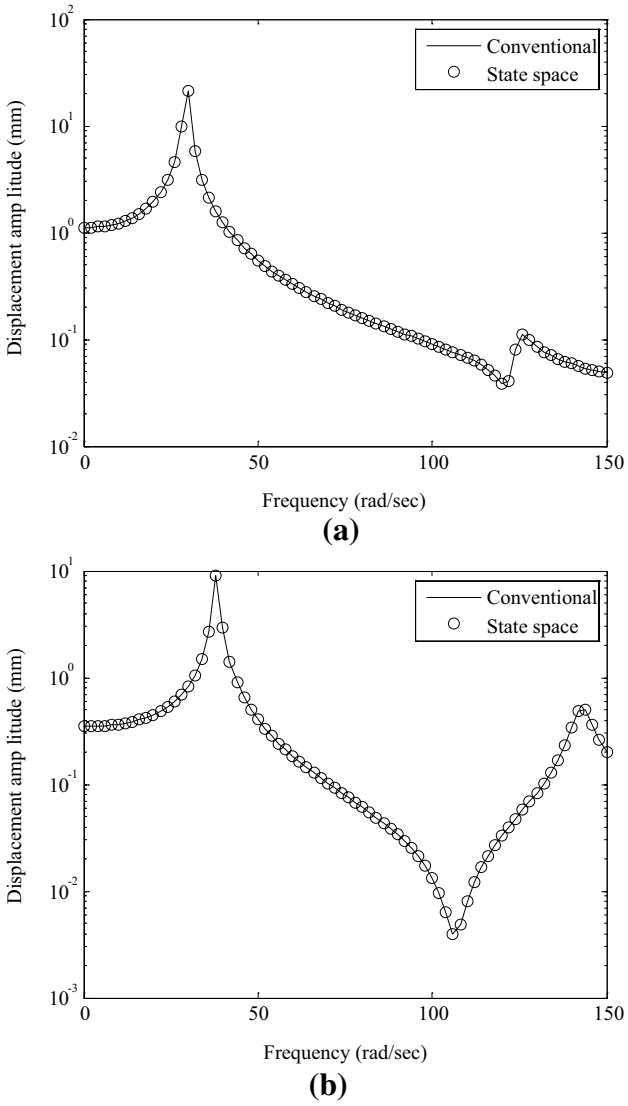

Fig. 7 Frequency response computed using conventional frequency-dependent storage modulus and loss coefficient and state space viscoelastic model with additional degrees of freedom for **a** rotor-disc system 1, **b** rotor-disc system 2 using PPC as shaft material

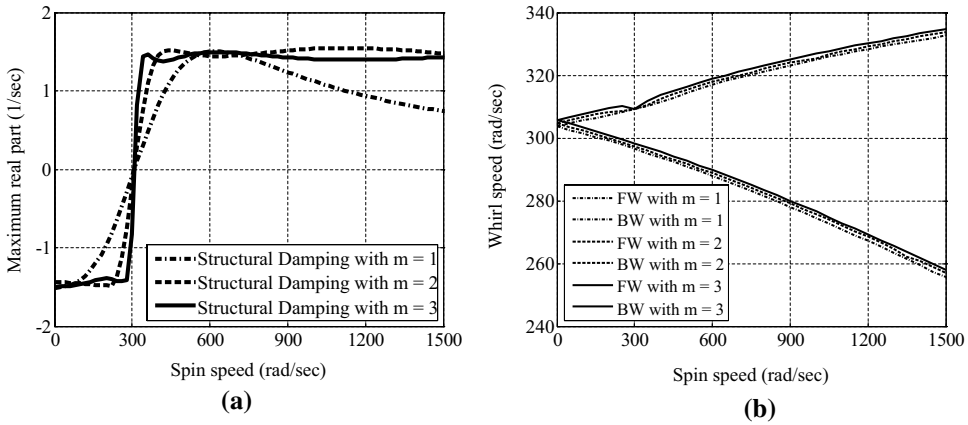

Fig. 8 Rotor-disc system 1 with structural damping comparing the results obtained using 1, 2 and 3 parallel branches, respectively: **a** the largest real part of the eigenvalues is plotted against spin speed and **b** Campbell Diagram for the first mode

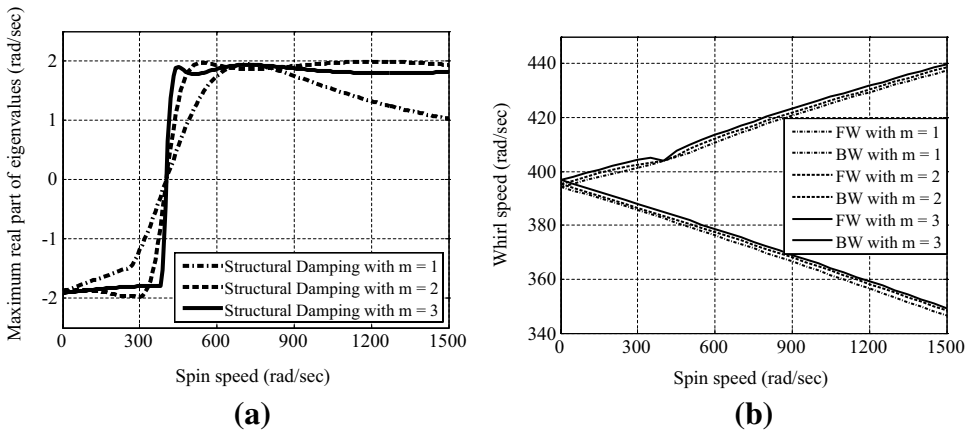

Fig. 9 Rotor-disc system 2 with structural damping comparing the results obtained using 1, 2 and 3 parallel branches, respectively: **a** the largest real part of the eigenvalues is plotted against spin speed and **b** Campbell Diagram for the first mode

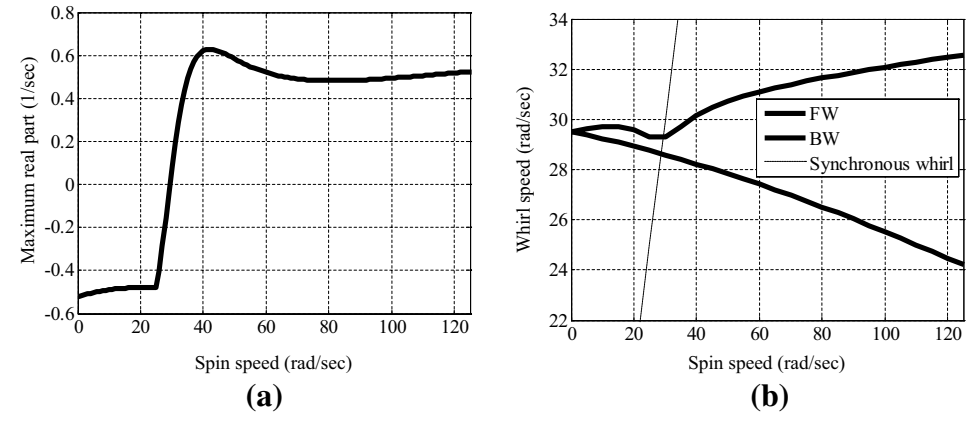

Fig. 10 Rotor-disc system 1 with PPC as shaft material: **a** the largest real part of the eigenvalues is plotted against spin speed and **b** Campbell Diagram for the first mode

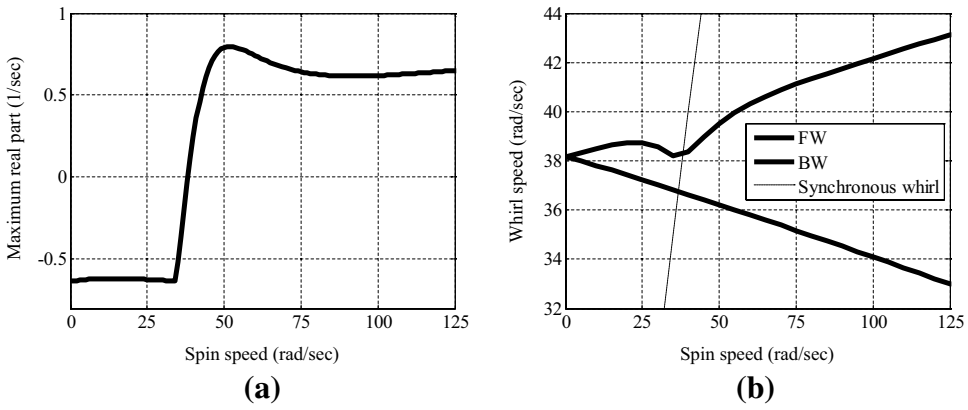

Fig. 11 Rotor-disc system 2 with PPC as shaft material: **a** the largest real part of the eigenvalues is plotted against spin speed and **b** Campbell Diagram for the first mode

For the viscoelastic material PPC, three parallel Maxwell branches are used. The systems become unstable beyond the first forward synchronous critical speed as in the previous case (Figs. 10, 11).

The time response of the rotor-disc systems is computed using Eq. (22) under two different force excitations: a horizontal unit step input (1 N) and a unit unbalance (1 N) at the location of the disc (left disc for system 2). In each case two spin speeds are considered: one in the subcritical stable zone and another in the supercritical unstable zone. The horizontal and vertical displacements and the rotor orbit at the location of the disc are plotted in inertial frame. In addition, the Fast Fourier Transform (FFT) of time response is presented. The same rotor-disc systems are tried to illustrate the results considering both structural damping and viscoelastic behaviour.

The response of rotor-disc system 1, using mild steel as rotor material in both subcritical and supercritical conditions, to the horizontal unit step input is depicted in Figs. 12 and 13 respectively. The subcritical response is stable with the vibration amplitude dying out with time but the supercritical response is unstable as expected with the vibration amplitude increasing with time resulting in an ever increasing whirl orbit. The FFT shows the presence of both the forward and backward whirl modes with the former largely dominating the later in supercritical response. Since the backward and forward whirl frequencies are close, beating is seen in the time response (Fig. 12a).

The response of rotor-disc system 2, in both subcritical and supercritical conditions, to the horizontal unit step input is depicted in Figs. 14 and 15 respectively. The patterns and trends are similar to those seen in the case of rotor-disc model 1 with the supercritical response showing instability.

The response of rotor-disc system 1, using mild steel as rotor material in both subcritical and supercritical conditions, to the 1 N unbalance is depicted in Figs. 16 and 17 respectively. The unbalance force acts like harmonic excitations in two mutually perpendicular transverse planes. The subcritical response is stable while the supercritical response is unstable as expected. The FFT shows that in subcritical response the forcing frequency dominates over the forward whirl mode. The forward mode slowly gets damped out. But in supercritical response the forward whirl mode becomes much more prominent. It is known that for material damping the forward mode becomes unstable and grows with time. The unstable response becomes much larger in comparison with the unbalance response.

The response of rotor-disc system 2, in both subcritical and supercritical conditions, to the 1 N unbalance is shown in Figs. 18 and 19 respectively. The patterns and trends are

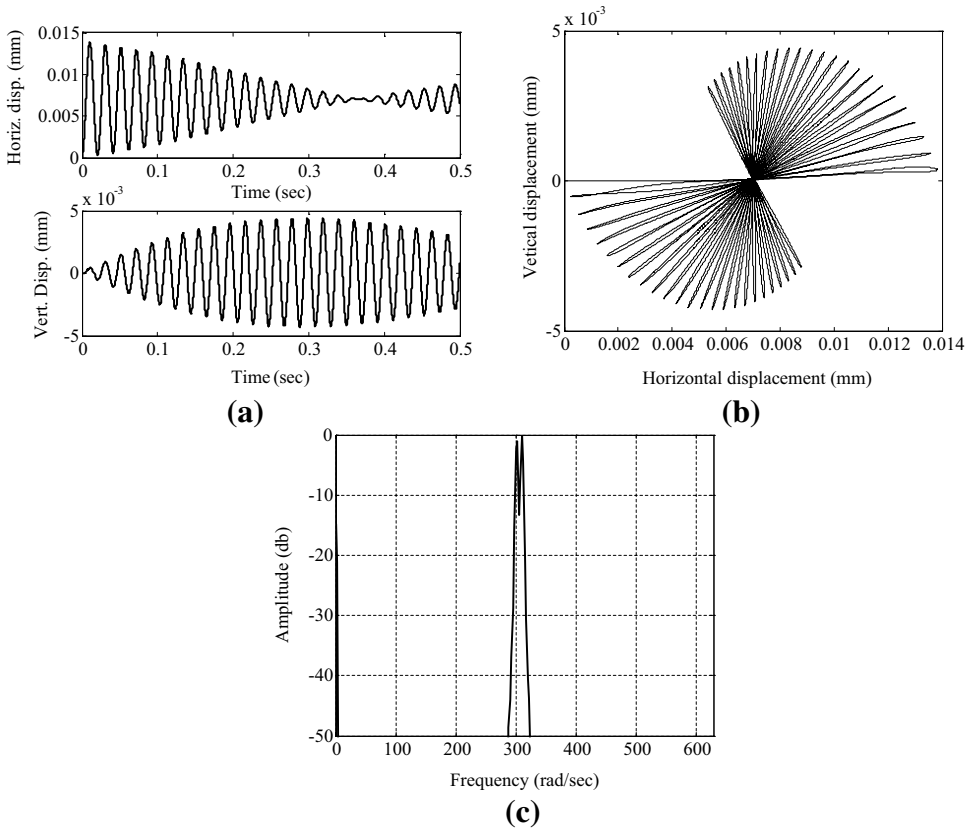

Fig. 12 Time response to a horizontal unit step input (1 N) applied at the location of the disc, showing **a** displacement, **b** Whirl orbit and **c** FFT of rotor-disc system 1 with mild steel shaft undergoing structural damping at a spin speed of 200 rad/s (subcritical zone)

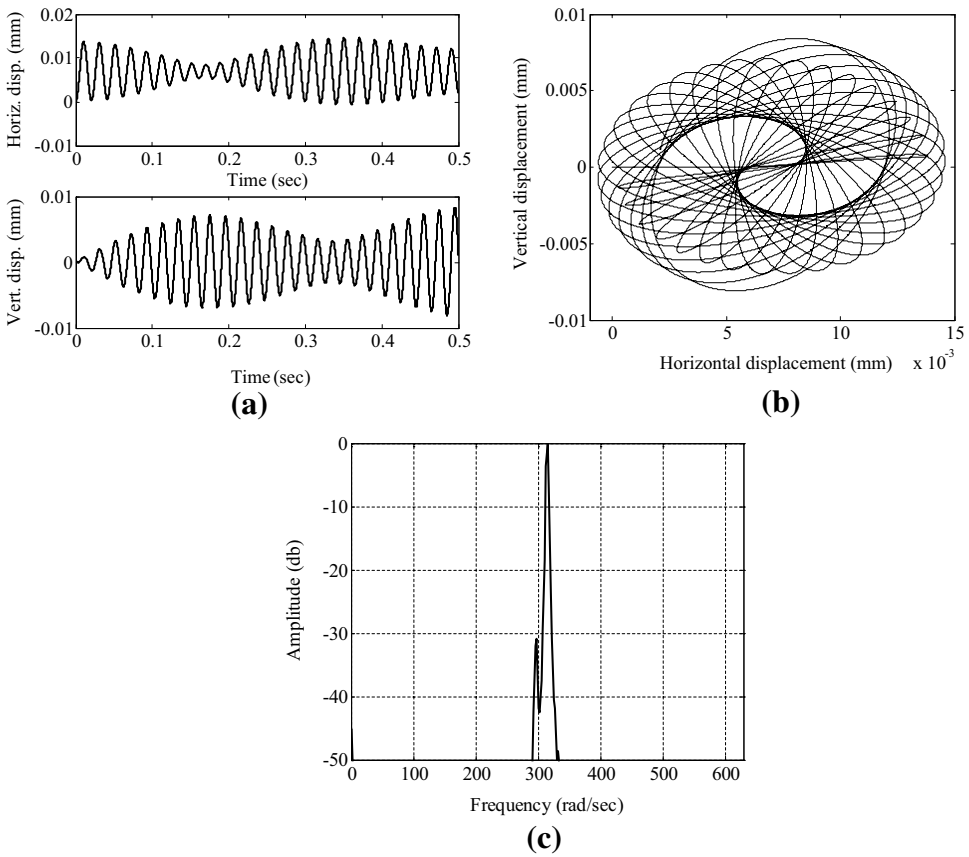

Fig. 13 Time response to a horizontal unit step input (1 N) applied at the location of the disc, showing **a** displacement, **b** Whirl orbit and **c** FFT of rotor-disc system 1 with mild steel shaft undergoing structural damping at a spin speed of 500 rad/s (supercritical zone)

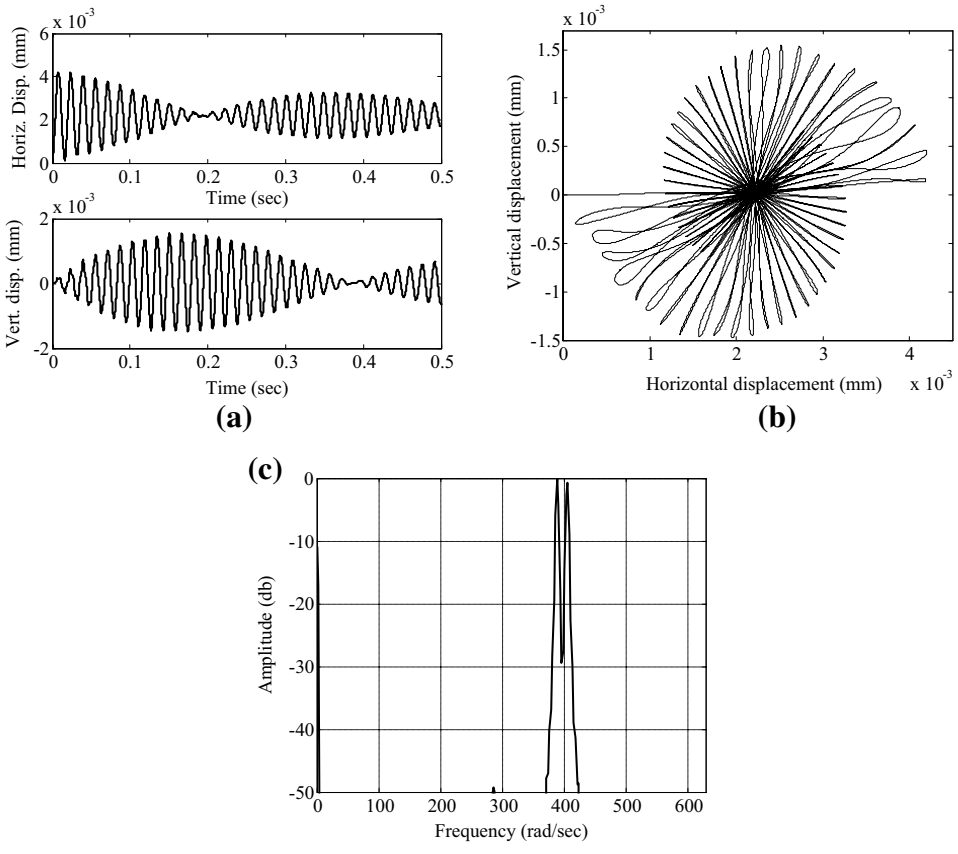

Fig. 14 Time response to a horizontal unit step input (1 N) applied at the location of the left disc, showing **a** displacement, **b** Whirl orbit and **c** FFT of rotor-disc system 2 with mild steel shaft undergoing structural damping at a spin speed of 300 rad/s (subcritical zone)

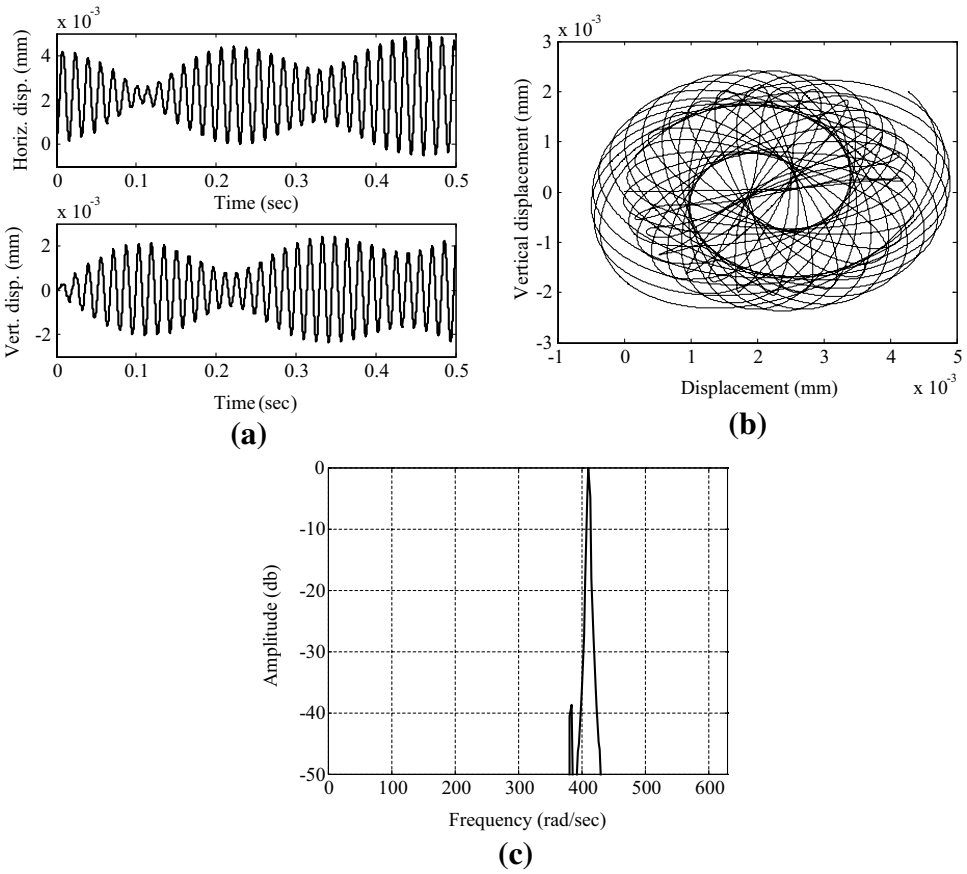

Fig. 15 Time response to a horizontal unit step input (1 N) applied at the location of the left disc, showing **a** displacement, **b** Whirl orbit and **c** FFT of rotor-disc system 2 with mild steel shaft undergoing structural damping at a spin speed of 500 rad/s (supercritical zone)

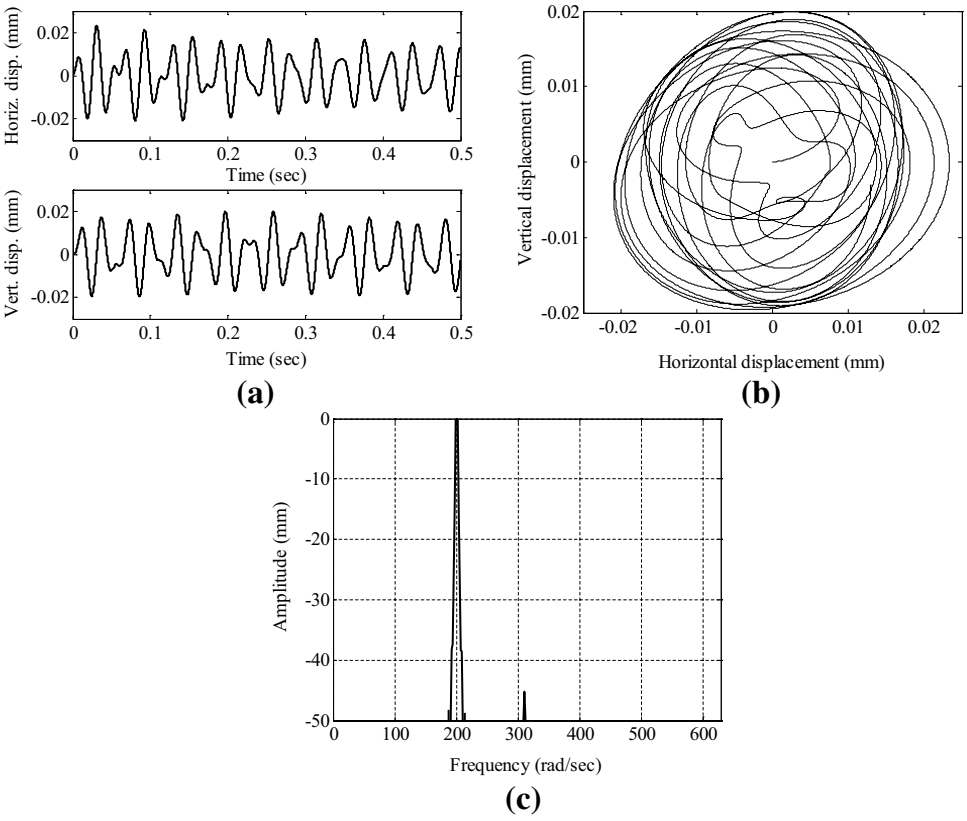

Fig. 16 Time response to a unit unbalance (1 N) applied at the location of the disc, showing **a** displacement, **b** Whirl orbit and **c** FFT of rotor-disc system 1 with mild steel shaft undergoing structural damping at a spin speed of 200 rad/s (subcritical zone)

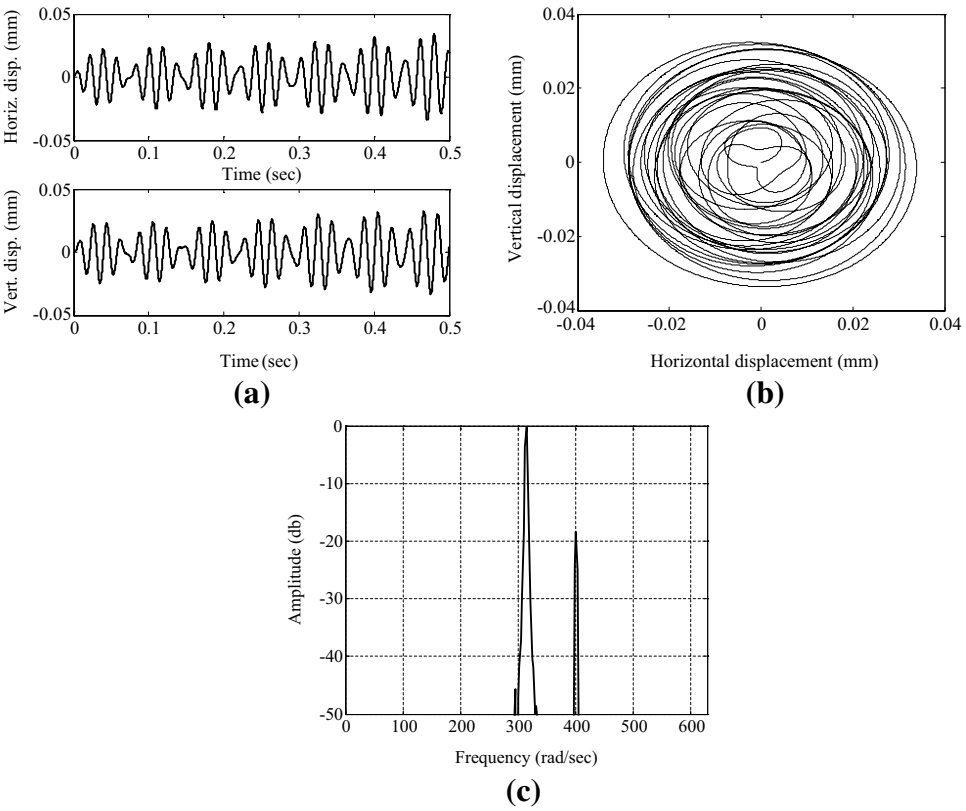

Fig. 17 Time response to a unit unbalance (1 N) applied at the location of the disc, showing **a** displacement, **b** Whirl orbit and **c** FFT of rotor-disc system 1 with mild steel shaft undergoing structural damping at a spin speed of 400 rad/s (supercritical zone)

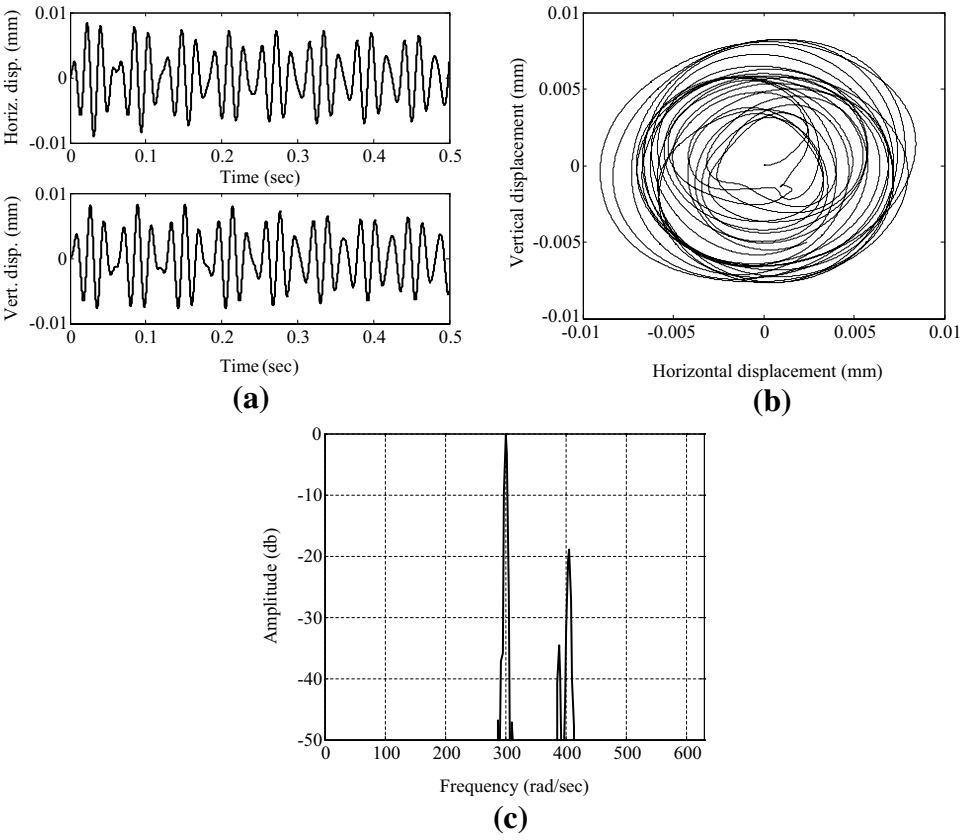

Fig. 18 Time response to a unit unbalance (1 N) applied at the location of the left disc, showing **a** displacement, **b** Whirl orbit and **c** FFT of rotor-disc system 2 with mild steel shaft undergoing structural damping at a spin speed of 300 rad/s (subcritical zone)

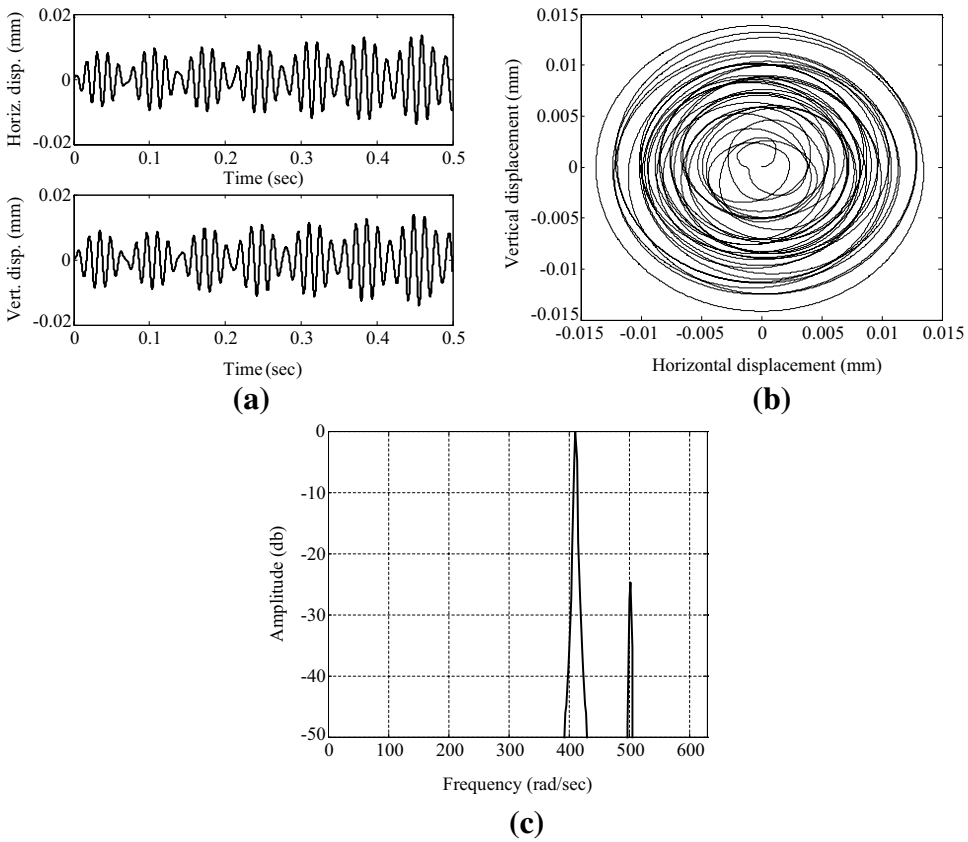

Fig. 19 Time response to a unit unbalance (1 N) applied at the location of the left disc, showing **a** displacement, **b** Whirl orbit and **c** FFT of rotor-disc system 2 with mild steel shaft undergoing structural damping at a spin speed of 500 rad/s (supercritical zone)

similar to those seen in the case of rotor-disc model 1 with the supercritical response showing instability.

The response of rotor-disc system 1, using PPC as shaft materials in both subcritical and supercritical conditions, to the horizontal unit step input (1 N) is shown in Figs. 20 and 21 respectively. The subcritical response is stable with the vibration amplitude dying out with time but the supercritical response is unstable as expected with the vibration amplitude increasing with time resulting in a growing whirl orbit. The FFT shows the presence of only the forward whirl mode in both subcritical and supercritical response of PPC. This can be attributed to the higher material damping of PPC as compared to mild steel. In the supercritical response the system becomes unstable at the forward whirl mode.

The response of rotor-disc system 2, PPC as rotor material in both subcritical and supercritical conditions, to the horizontal unit step input (1 N) is depicted in Figs. 22 and 23 respectively. The patterns and trends are same as seen in the case of rotor-disc system 1 with the supercritical response demonstrating instability.

The response of rotor-disc system 1, with PPC as shaft material in both subcritical and supercritical conditions, to the 1 N unbalance is depicted in Figs. 24 and 25 respectively. The subcritical response is stable while the supercritical response is unstable as expected. The FFT shows the presence of synchronous whirl frequency as well as the forward natural frequency at that synchronous spin speed. In subcritical response the forcing frequency dominates over the forward whirl mode. The forward mode slowly gets damped out. But in supercritical response the forward whirl mode becomes much more prominent. It is known that for material damping the forward mode becomes unstable and grows with time. The unstable response becomes much larger in comparison with the unbalance response.

The response of rotor-disc system 2, using ABS and PPC as rotor material in both subcritical and supercritical conditions, to the 1 N rotating unbalance is depicted in Figs. 26 and 27 respectively.

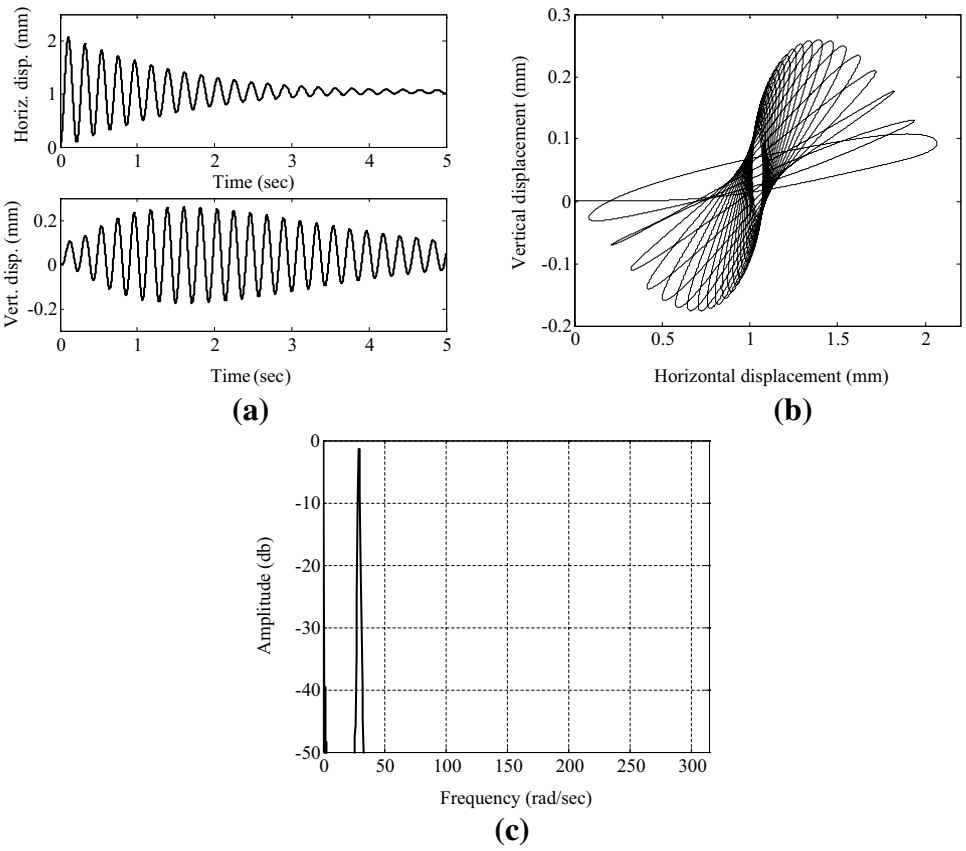

Fig. 20 Time response to a horizontal unit step input (1 N) applied at the location of the disc, showing **a** displacement, **b** Whirl orbit and **c** FFT of rotor-disc system 1 with viscoelastic PPC shaft at a spin speed of 20 rad/s (subcritical zone)

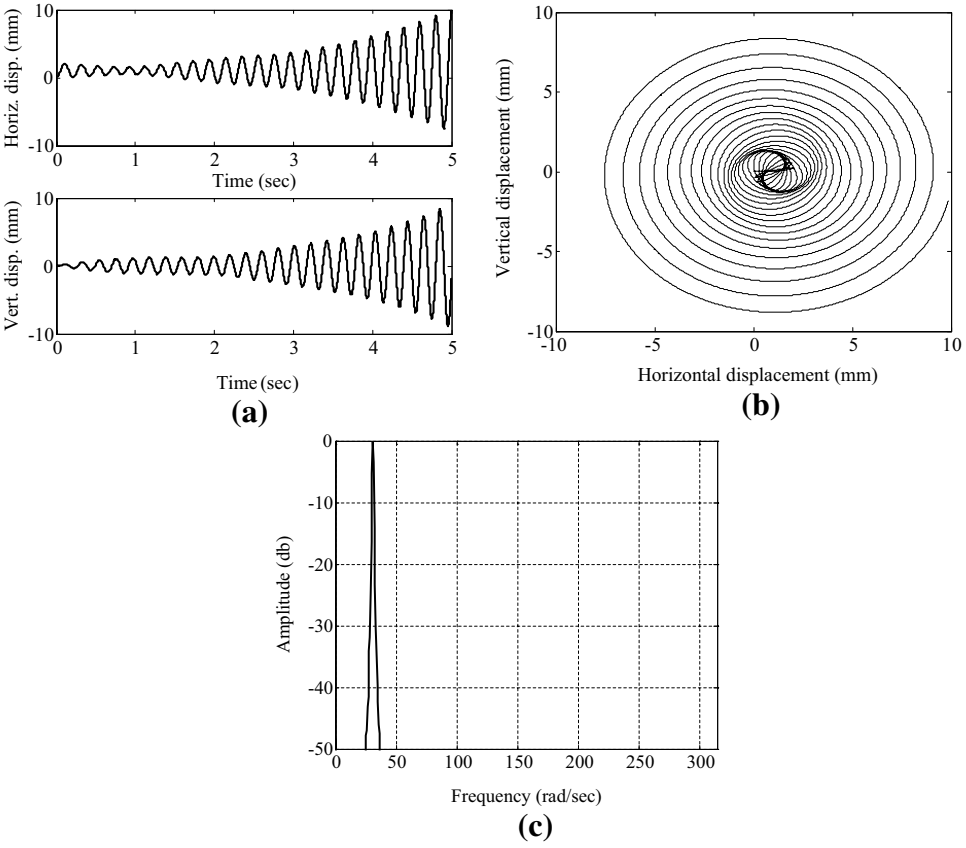

Fig. 21 Time response to a horizontal unit step input (1 N) applied at the location of the disc, showing **a** displacement, **b** Whirl orbit and **c** FFT of rotor-disc system 1 with viscoelastic PPC shaft at a spin speed of 50 rad/s (supercritical zone)

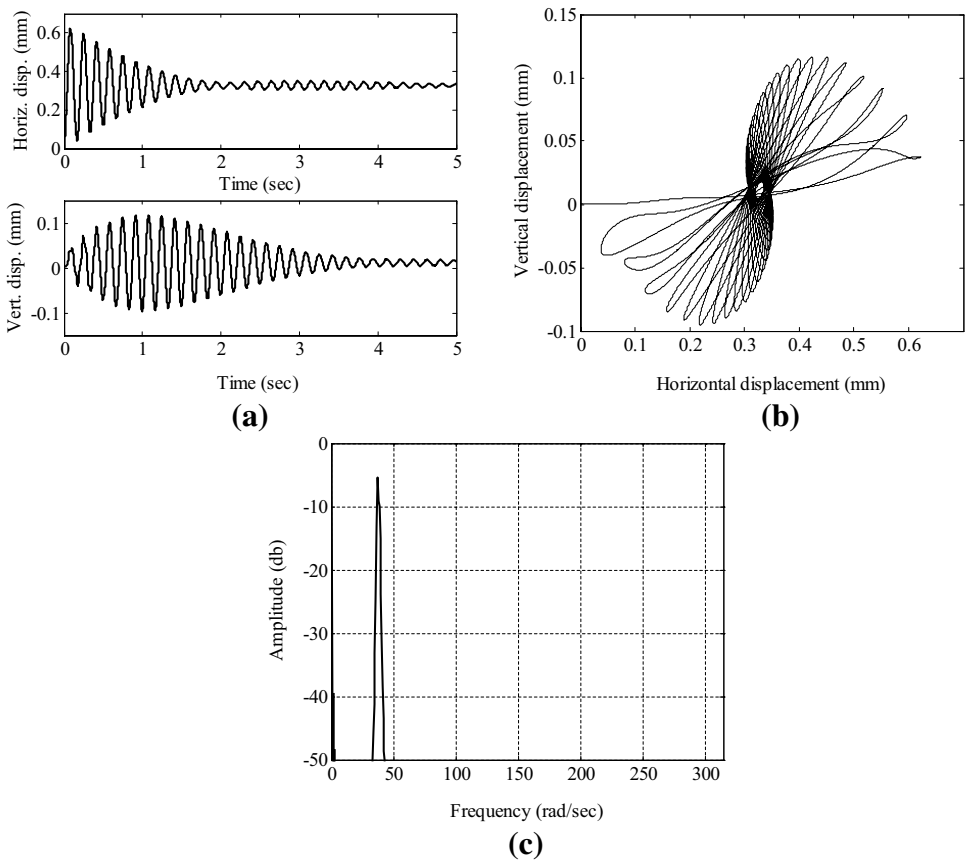

Fig. 22 Time response to a horizontal unit step input (1 N) applied at the location of the left disc, showing **a** displacement, **b** Whirl orbit and **c** FFT of rotor-disc system 2 with viscoelastic PPC shaft at a spin speed of 30 rad/s (subcritical zone)

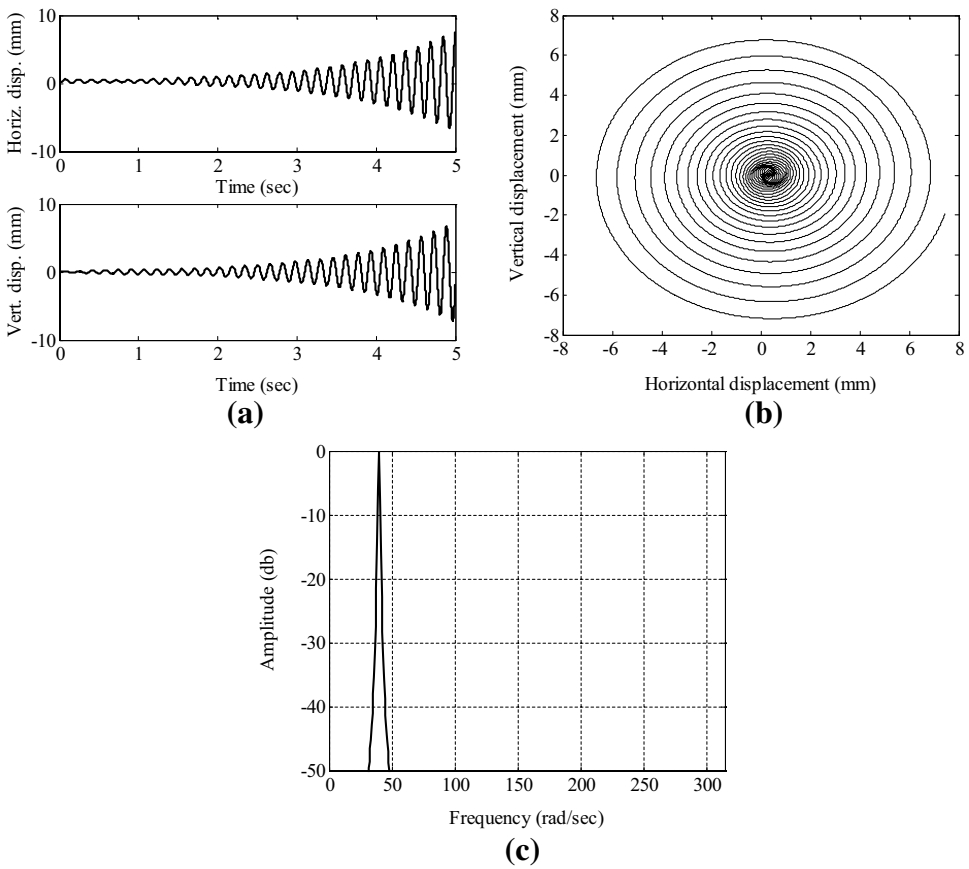

Fig. 23 Time response to a horizontal unit step input (1 N) applied at the location of the left disc, showing **a** displacement, **b** Whirl orbit and **c** FFT of rotor-disc system 2 with viscoelastic PPC shaft at a spin speed of 50 rad/s (supercritical zone)

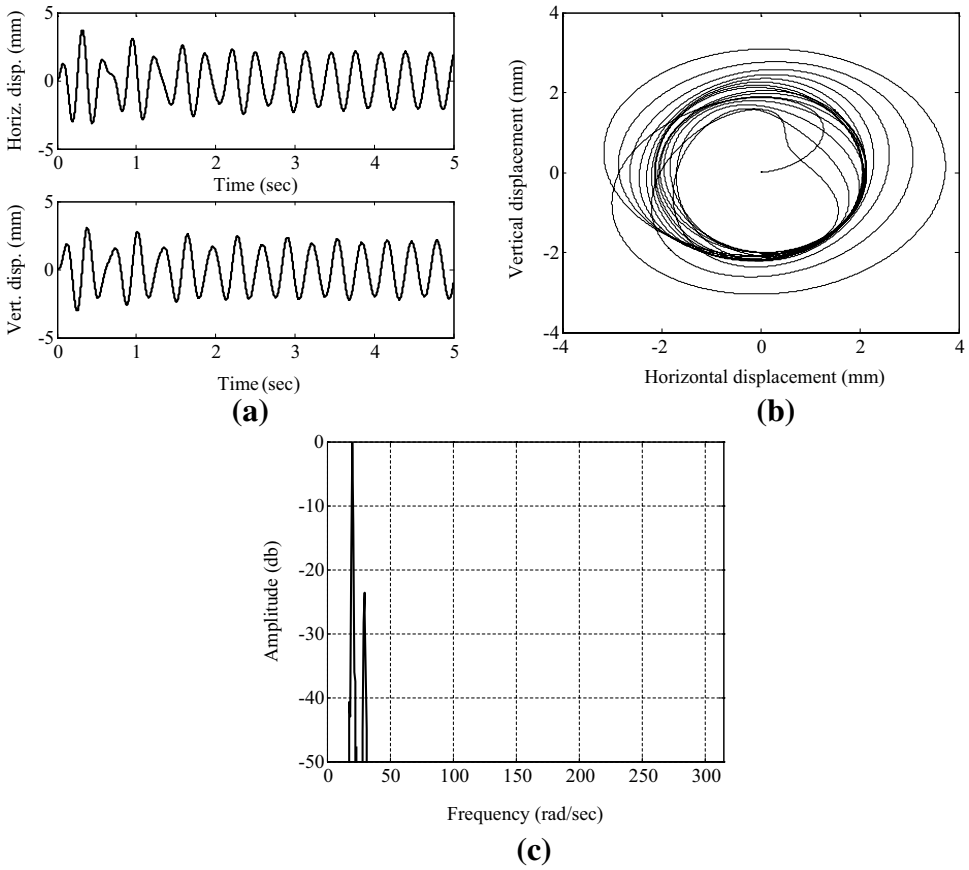

Fig. 24 Time response to a unit unbalance (1 N) applied at the location of the disc, showing **a** displacement, **b** Whirl orbit and **c** FFT of rotor-disc system 1 with viscoelastic PPC shaft at a spin speed of 20 rad/s (subcritical zone)

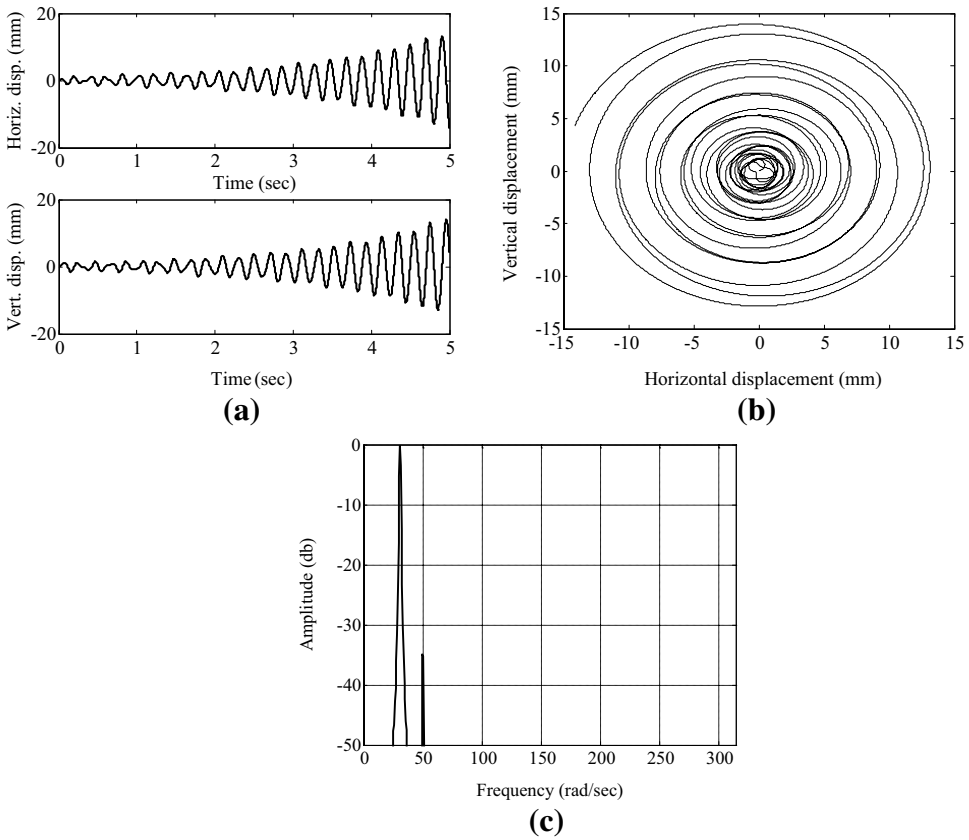

Fig. 25 Time response to a unit unbalance (1 N) applied at the location of the disc, showing **a** displacement, **b** Whirl orbit and **c** FFT of rotor-disc system 1 with viscoelastic PPC shaft at a spin speed of 50 rad/s (supercritical zone)

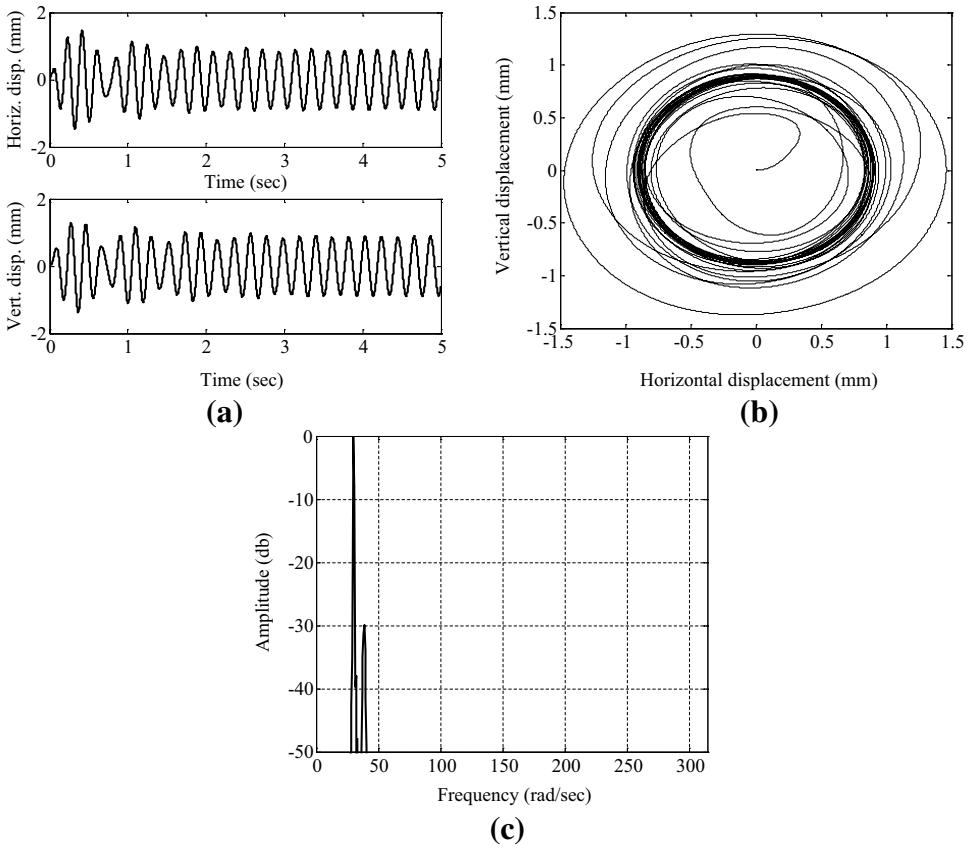

Fig. 26 Time response to a unit unbalance (1 N) applied at the location of the left disc, showing **a** displacement, **b** Whirl orbit and **c** FFT of rotor-disc system 2 with viscoelastic PPC shaft at a spin speed of 30 rad/s (subcritical zone)

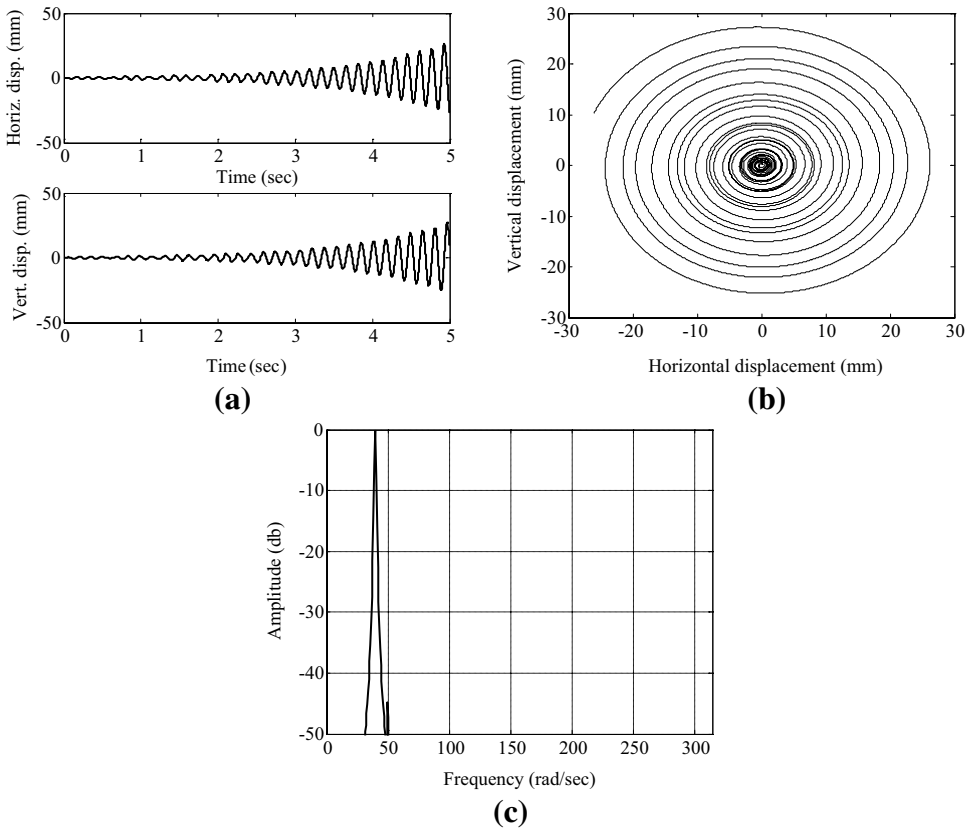

Fig. 27 Time response to a unit unbalance (1 N) applied at the location of the left disc, showing **a** displacement, **b** Whirl orbit and **c** FFT of rotor-disc system 2 with viscoelastic PPC shaft at a spin speed of 50 rad/s (supercritical zone)

Conclusion

A rotating shaft element based on the Euler–Bernoulli beam element and Maxwell–Wiechert material model is presented. This element is believed to be useful for time-domain analysis of rotors with structural and frequency dependent damping. For typical viscoelastic materials the parameters for the Maxwell–Wiechert model can be extracted from experimental data obtained through testing of standard specimen. However, in case of structural damping the parameters can be obtained by solving algebraic equations. The element stiffness and mass matrices obtained for an elastic shaft element of unit modulus of elasticity and density can be appended to obtain the state space matrices for the viscoelastic one. The element equations have to be assembled in state space considering velocity degrees of freedom and damping degrees of freedom besides the usual nodal degrees of freedom.

References

1. Liu F, Li-Q Chen (2008) Complex modal analysis for vibration of damped continua. Adv Vib Eng 7(3):283–291
2. Bhangale RK, Ganesan N (2007) Vibration and damping behavior of a viscoelastic functionally graded sandwich plate. Adv Vib Eng 6(4):333–341
3. Ramachandra Reddy BN, Roja Rani P, Badari Narayana K (2007) Visco-elastic damping with composite constraining layers. Adv Vib Eng 6(4):321–332
4. Gounaris GD, Nikolakopoulos PG, Papadopoulos CA (2014) Hysteretic damping and stress evaluation of rotor-bearing systems in the resonance zone. J Vib Eng Technol 2(2):171–189
5. Nakra BC, Chawla DR (1971) Shock response of a three-layer sandwich beam with viscoelastic core. J Aeronaut Soc India 23(3):135–139
6. Dutt JK, Roy H (2011) Viscoelastic modeling of rotor-shaft systems using an operator-based approach. J Mech Eng Sci 225(1):73–87
7. Genta G, Bassani D, Delprete C (1996) DYNROT: a finite element code for rotordynamic analysis based on complex coordinates. Eng Comput 13(6):86–109
8. Bagley RL, Torvik BJ (1983) Fractional calculus—a different approach to finite element analysis of viscoelastic damped structures. AIAA J 21(5):741–748
9. Friswell MI, Dutt JK, Adhikari S, Lees AW (2010) Time domain analysis of a viscoelastic rotor using internal variable models. Int J Mech Sci 52(10):1319–1324
10. Roy H, Dutt JK, Datta PK (2013) Dynamic behavior of stepped multilayered viscoelastic beams—a finite element approach. Adv Vib Eng 12(1):75–88
11. Roy H, Dutt JK, Chandraker S (2014) Modeling of multilayered viscoelastic rotors—an operator based approach. J Vib Eng Technol 2(6):485–494
12. Golla DF, Hughes PC (1985) Dynamics of viscoelastic structures—a time domain finite element formulation. J Appl Mech 52:897–906
13. McTavish DJ, Hughes PC (1993) Modeling of linear viscoelastic space structures. J Vib Acoust 115:103–110
14. Adhikari S (2001) Eigenrelations for non-viscously damped systems. AIAA J 39:1624–1630
15. Adhikari S (2002) Dynamics of non-viscously damped linear systems. J Eng Mech 128:328–339
16. Wagner N, Adhikari S (2003) Symmetric state-space formulation for a class of non-viscously damped systems. AIAA J 41:951–956
17. Adhikari S, Wagner N (2003) Analysis of a symmetric non-viscously damped linear dynamic system. J Appl Mech 70:885–893
18. Adhikari S (2005) Qualitative dynamic characteristics of a non-viscously damped oscillator. Proc R Soc Lond Ser A 461:2269–2288
19. Adhikari S (2008) Dynamic response characteristics of a non-viscously damped oscillator. J Appl Mech 75:011003:1–12
20. Genta G, Amati N (2010) Hysteretic damping in rotordynamics: an equivalent formulation. J Sound Vib 329:4772–4784
21. Nelson HD, McVaugh JM (1976) The dynamics of rotor-bearing systems using finite elements. ASME J Eng Industry 98(2):593–600
22. Genta G (2009) Vibration dynamics and control. Springer, New York